

Article

Estimating Evapotranspiration from an Improved Two-Source Energy Balance Model Using ASTER Satellite Imagery

Qifeng Zhuang and Bingfang Wu *

Received: 27 August 2015; Accepted: 19 November 2015; Published: 26 November 2015

Academic Editor: Assefa M. Melesse

Institute of Remote Sensing and Digital Earth (RADI), Chinese Academy of Sciences, Beijing 100094, China; zhuangqf@radi.ac.cn

* Correspondence: wubf@radi.ac.cn; Tel.: +86-10-6485-5689; Fax: +86-10-6485-8721

Abstract: Reliably estimating the turbulent fluxes of latent and sensible heat at the Earth's surface by remote sensing is important for research on the terrestrial hydrological cycle. This paper presents a practical approach for mapping surface energy fluxes using Advanced Spaceborne Thermal Emission and Reflection Radiometer (ASTER) images from an improved two-source energy balance (TSEB) model. The original TSEB approach may overestimate latent heat flux under vegetative stress conditions, as has also been reported in recent research. We replaced the Priestley-Taylor equation used in the original TSEB model with one that uses plant moisture and temperature constraints based on the PT-JPL model to obtain a more accurate canopy latent heat flux for model solving. The collected ASTER data and field observations employed in this study are over corn fields in arid regions of the Heihe Watershed Allied Telemetry Experimental Research (HiWATER) area, China. The results were validated by measurements from eddy covariance (EC) systems, and the surface energy flux estimates of the improved TSEB model are similar to the ground truth. A comparison of the results from the original and improved TSEB models indicates that the improved method more accurately estimates the sensible and latent heat fluxes, generating more precise daily evapotranspiration (ET) estimate under vegetative stress conditions.

Keywords: surface energy fluxes; evapotranspiration; TSEB; satellite images; eddy covariance

1. Introduction

Modeling surface energy fluxes on a regional scale is essential for assessing energy and mass exchanges between the hydrosphere, atmosphere, and biosphere. Evapotranspiration (ET) is a major component of the processes and models for predicting soil water availability, forecasting rainfall, and monitoring drought, water balance, and global climate change [1]. However, ET is difficult to measure and predict, especially on a regional scale. Remote sensing techniques have been widely used to estimate surface energy fluxes in recent years because they provide numerous parameters necessary for surface energy balance (SEB) models, such as the land surface temperature, surface albedo, and vegetation index at various spatiotemporal resolutions.

The numerous SEB algorithms that have been developed in the past few decades generally include one-source models, such as SEBAL [2], METRIC [3], and SEBS [4], and multi-source models, such as TSEB [5] and SEB-4S [1]. The one-source models treat the vegetation and soil as one “big leaf” with identical temperature and aerodynamic resistance for heat transfer at the same height. In contrast are the multi-source models, in which vegetation and soil are independent sinks or sources of heat fluxes. Although good results have been obtained for dense canopies, the precision of one-source models always decreases over sparse vegetation [6,7]. Under partial vegetation canopy

cover, both soil and vegetation components contribute to the net flux exchange as well as the remotely sensed signals; multi-source approaches are more suitable in such situations. The two-source energy balance (TSEB) models can be divided into layer and patch approaches. The TSEB layer approach (e.g., [5]) is meant to represent a stand of vegetation exchanging sensible and latent heat with the atmosphere from two different sources: a substrate (e.g., bare soil or herbaceous canopy) and an upper canopy. The total flux of sensible or latent heat emanating from the whole canopy is calculated as the simple sum of the fluxes emanating from each layer [8]. In the TSEB patch model, each patch acts independently, and the total flux of sensible or latent heat is computed as the mean of the component fluxes (soil and canopy) weighted by their relative area (fractional vegetation cover, f_c) [8].

Both the layer and patch TSEB approaches require the input of the component temperatures (soil and canopy temperatures), which can be derived from the radiometric temperatures measured at two view angles, for example, using an along-track scanning radiometer (ATSR). However, radiometric temperature (T_{rad}) is usually only available at a single view angle from satellites (e.g., MODIS, ASTER, HJ-1B, FY3A, and Landsat 8). To solve this problem, the TSEB patch model proposed by Sanchez *et al.* [9] was tested by component temperatures from field observations; Anderson *et al.* [10] used the light-use-efficiency (LUE) model for TSEB scheme driven primarily by thermal remote sensing inputs. Long and Singh [11] proposed the TTME patch model and obtained the component temperatures from the sketch of the trapezoid f_c - T_{rad} feature space. The Priestley-Taylor iteration approach, which derives the component temperature by providing an initial estimate of the canopy ET, is more popular [12,13] due to its avoidance of having to estimate vapor pressure deficit and its brevity.

However, there are still deficiencies in regional applications using TSEB models, mostly resulting from the uncertainty of the derived component sensible and latent heat fluxes. Although the Priestley-Taylor iteration approach has been widely used in TSEB models, its insufficiency is obvious; it may overestimate the canopy ET, which leads to underestimation of the total sensible heat flux and overestimation of the total latent heat flux. This is especially the case with low soil wetness, high air drying power, and sparse vegetation cover [11,13–15] because the original Priestley-Taylor iteration approach proposed by Norman *et al.* [5] did not include a reasonable reduction of initial canopy ET under vegetative stress conditions, such as water stress and air temperature stress.

In this paper, an improved layer TSEB model was tested by combining four ASTER remote sensing images and micrometeorological flux tower data. A modified Priestley-Taylor iteration approach containing two plant physiological constraints, plant moisture and temperature, was introduced to provide a reasonable initial canopy ET for model solving. To map the daily ET, a method of extrapolation by combining the instantaneous evaporative fraction (EF) derived from ASTER images was used. Finally, the estimations were validated by covariance (EC) system measurements from nine stations over croplands in the Heihe Watershed Allied Telemetry Experimental Research (HiWATER) area, China. The estimations provided by the TSEB models with or without plant physiological constraints were also compared.

2. Materials and Methods

2.1. Study Site and Measurements

Accurate and precise ground-based measurements are essential for defining and verifying satellite-based estimates and for supporting specialized research [16]. HiWATER has been designed as a comprehensive eco-hydrological experiment in the Heihe River Basin in the arid northwest region of China within the framework of “Integrated research on the eco-hydrological process”. The overall objective of HiWATER is to improve the observability of hydrological and ecological processes, to build a world-class watershed observing system, and to enhance the applicability of remote sensing in integrated eco-hydrological studies and water resource management at the basin scale. Ground-based

measurements from nine stations were collected in 2012 within an observation matrix (Figure 1) located in the Yingke and Daman irrigation districts of the Zhangye Oasis. The land surface of the observation area is heterogeneously dominated by corn, orchards, and vegetables. Each station was equipped with an EC tower and an automatic weather system (AWS).

The AWS observations (Figure 2) included wind speed (height: 5 m and 10 m; sensor type: AV-30 WS (Avalon Scientific, Inc., Jersey, NJ, USA), Windsonic (Gill Instruments Ltd., Hampshire, UK)), air temperature and humidity (height: 5 m and 10 m; sensor type: Avalon AV-14TH (Avalon Scientific, Inc., Jersey, NJ, USA)), air pressure, net radiation (R_n) and four radiation components (downward shortwave radiation, reflected shortwave radiation, downward longwave radiation, and upward longwave radiation; sensor type: Kipp & Zonen CNR 4 (Kipp & Zonen B.V., Delft, The Netherlands), Eppley PIR & PSP (Eppley Laboratory, Inc., Newport, RI, USA), soil temperature (sensor type: Avalon AV-10T (Avalon Scientific, Inc., Jersey, NJ, USA)) and moisture (sensor type: Campbell CS616 (Campbell Scientific, Logan, UT, USA)) profiles, and turbulent fluxes (sensor type: CSAT3 & LI7500A (Campbell Scientific, Logan, UT, USA)). Three soil heat flux plates (sensor type: AV-HFT3 (Avalon Scientific, Inc., Jersey, NJ, USA)) were placed horizontally 0.06 m below the soil surface, one under the plant positions and two in adjacent rows. The soil heat flux (G) was calculated by adding the average flux measured by the three soil heat flux plates at a fixed depth (0.06 m) to the energy stored in the soil layer above the heat flux (Δs) plate measured using two thermocouples buried 0.02 m and 0.04 m over the flux plates. The net storage of energy (Δs) in the soil column was computed using the change over time of the temperature of the soil layer above the heat flux plates via the method of Consoli and Vanella [16].

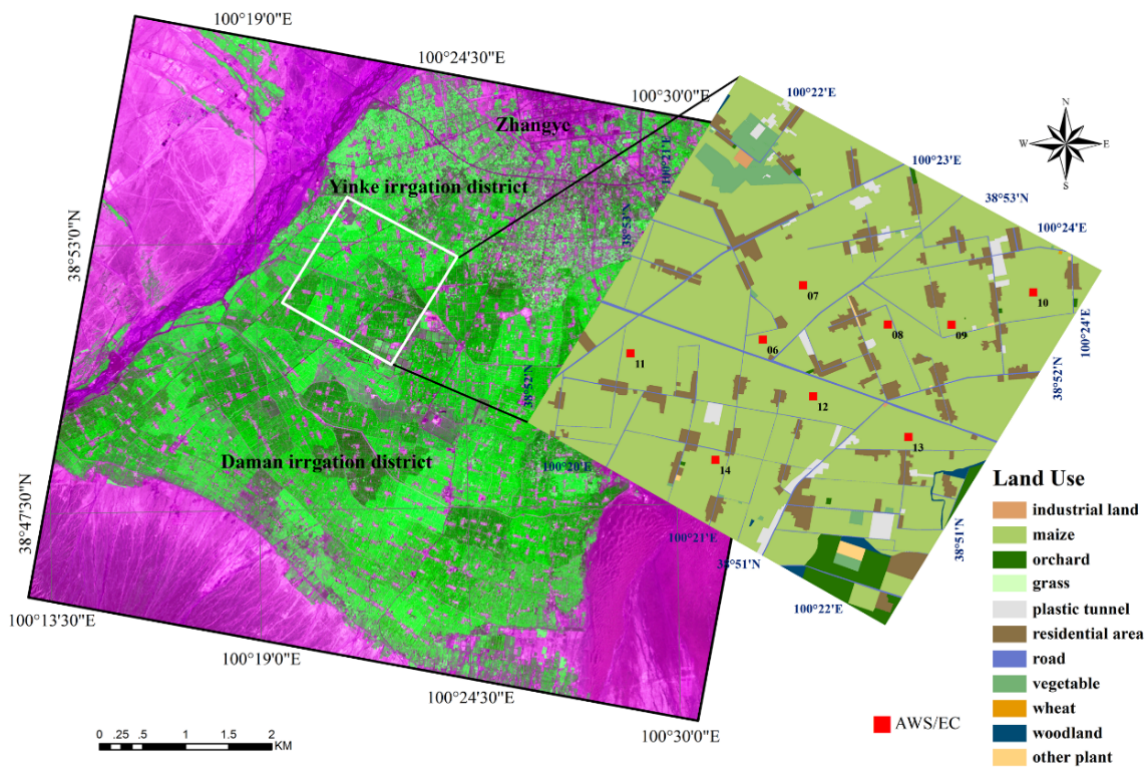


Figure 1. Land cover and the meteorological instrument locations in the study area.

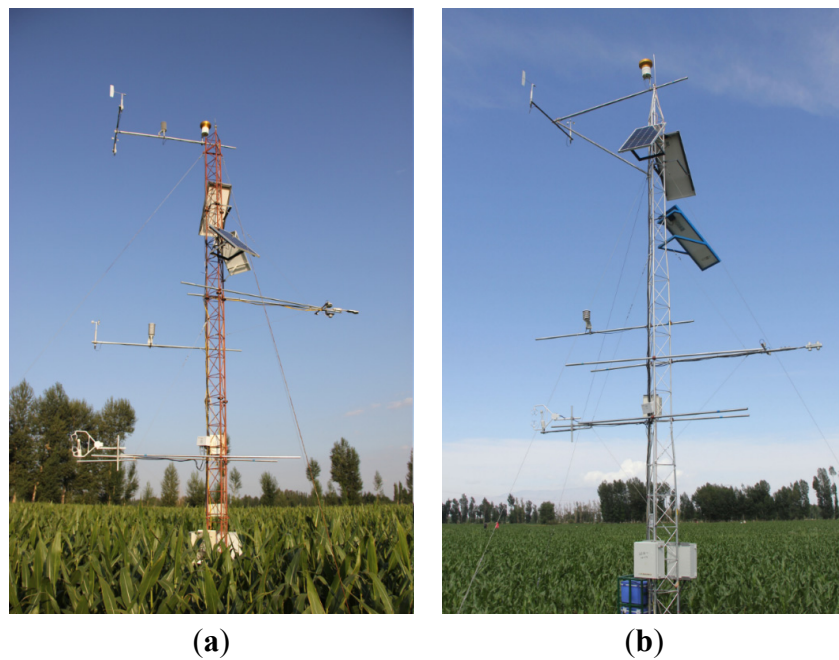


Figure 2. Two EC flux towers in the study area: EC08 (a) and EC11 (b).

The raw data acquired from the EC towers at 10 Hz were processed using the post-processing software EdiRe developed by Edinburgh University, UK, including spike removal, lag correction of H_2O/CO_2 relative to the vertical wind component, sonic virtual temperature correction, performance of the planar fit coordinate rotation, density fluctuation correction (WPL-correction), and frequency response correction [17]. The half-hour-averaged latent and sensible heat flux (LE and H) values were calculated from the post-processed results. In general, the averaged closure ratio [$CR = (LE + H)/(R_n - G)$] for all observations was 0.85. Twine *et al.* [18] reported that the Bowen ratio method for forcing closure of the measured energy balance improved the agreement with the water balance results. Therefore, this method was used to correct the eddy covariance measurements of the sensible and latent heat fluxes for energy closure.

2.2. Remote Sensing Data

ASTER has three spectral bands in the visible near-infrared (VNIR), six bands in the short-wave infrared (SWIR), and five bands in the thermal infrared (TIR) regions, with 15, 30, and 90 m ground resolution, respectively. Four images from ASTER Level 1-B in 2012 were collected over the whole experimental region on 11 August, 18 August, 3 September, and 12 September. The images were geometrically rectified to the Universal Transversal Mercator projection system (UTM Zone 33N) using the Environment for Visualizing Images (ENVI). The spectral radiance was obtained through a radiometric calibration process for the calculation of the apparent reflectance in the VNIR region of the electromagnetic spectrum using the following equations:

$$L_\lambda = (DN_\lambda - 1) \cdot UCC_\lambda, \quad (1)$$

where L_λ is the ASTER spectral radiance ($W \cdot m^{-2} \cdot sr^{-1} \cdot \mu m^{-1}$) at the sensor's aperture at wavelength λ and obtained from the digital numbers (DN) values from the ASTER Level 1-B data. UCC_λ is the unit conversion coefficient. The surface reflectance was obtained from the at-sensor spectral radiance by atmospheric correction conducted using the ENVI Fast Line-of-sight Atmospheric Analysis of Spectral Hypercubes (FLAASH) method. The normalized difference vegetation index (NDVI) was

computed using the ASTER band 2 and 3N surface reflectance. The leaf area index (LAI) was related to NDVI based on the following equation [19]:

$$LAI = \sqrt{\frac{1 + NDVI}{1 - NDVI}} NDVI. \quad (2)$$

Surface radiometric temperature (T_{rad}) is a key parameter in the TSEB model. In this study, T_{rad} was retrieved using the algorithm for the linear combination of the ASTER five TIR bands proposed by Jimenez-Munoz and Sobrino [20].

Furthermore, the disaggregate radiometric temperature (DisTrad) approach proposed by Kustas *et al.* [21] was used to disaggregate T_{rad} to a 15 m spatial resolution, the same resolution as the VNIR region of ASTER. DisTrad is a thermal sharpening technique that uses the relationship between T_{rad} and NDVI without requiring any empirical external calibration by fitting a least-squares expression between the radiometric temperature and NDVI (15 m) aggregated at the coarser T_{rad} spatial resolution (90 m). This technique has shown good performance for agricultural areas [16].

2.3. Methods

The improved TSEB model has a similar scheme to the model of Norman *et al.* [5]. The relationships between the net radiation (R_n), soil heat flux (G), sensible heat flux (H), and latent heat flux (LE) are:

$$R_n = G + H + LE \quad (3)$$

$$R_n = R_{nc} + R_{ns} \quad (4)$$

$$H = H_c + H_s \quad (5)$$

$$LE = LE_c + LE_s \quad (6)$$

$$G = C_g R_{ns} \quad (7)$$

$$R_{ns} = LE_s + H_s + G \quad (8)$$

$$R_{nc} = LE_c + H_c. \quad (9)$$

R_{nc} and R_{ns} are the net radiation ($W \cdot m^{-2}$) absorbed by the canopy and penetrating to the soil surface, respectively; H_c and H_s are the sensible heat fluxes ($W \cdot m^{-2}$) from vegetation and soil, respectively; and, similarly, LE_c and LE_s are the latent heat fluxes ($W \cdot m^{-2}$) over the canopy and soil surface, respectively. C_g is the ratio of soil heat flux and net radiation over the soil surface. A simple algorithm was used to predict the net radiation:

$$R_n = (1 - \alpha)S_d + \varepsilon_a \sigma T_a^4 - \varepsilon \sigma T_{rad}^4 \quad (10)$$

$$\varepsilon_a = 1.24 \left(\frac{e_a}{T_a} \right)^{1/7} \quad (11)$$

$$\varepsilon = f_c \varepsilon_c + (1 - f_c) \varepsilon_s, \quad (12)$$

where S_d is the downwelling shortwave radiation ($W \cdot m^{-2}$) estimated by Allen *et al.* [3] and ε_a is the emissivity of the atmosphere related to air temperature T_a (K) and water vapor pressure e_a (hPa). ε is the land surface emissivity estimated by Consoli and Vanella [16]. ε_c is the emissivity of vegetation and ε_s is the emissivity of the soil surface, which can depend on the soil moisture [11,22]. In addition, some representative values for ε_c and ε_s can be retrieved from the look-up tables compiled by Rubio *et al.* [23] in the absence of measured values. α is the broadband albedo in the visible and near infrared bands computed from the formulation proposed by Consoli *et al.* [24]. f_c is the fractional vegetation cover and is related to the NDVI.

The soil heat flux was estimated using the equation described by Colaizzi *et al.* [25]:

$$G = C_g R_{ns} = \left\{ a \cdot \cos \left[\frac{2\pi}{b} (t + c) \right] \right\} R_{ns}, \tag{13}$$

where t is the time in seconds relative to solar noon, a is the amplitude parameter, b is the period, and c is the phase shift. In this study, $a = 0.3$, $b = 86,400$ (s), and $c = 10,800$ (s).

The sensible heat flux is expressed according to the following equations:

$$H_c = \rho C_p \frac{T_c - T_a}{r_{ah}} \tag{14}$$

$$H_s = \rho C_p \frac{T_s - T_a}{r_{ah} + r_s}, \tag{15}$$

where T_c is the radiometric temperature from the canopy component and T_s is the radiometric temperature from the soil surface. The derived surface radiometric temperature T_{rad} can be related to T_c and T_s based on the fractional vegetation cover within the sensor field of view, $f(\theta)$:

$$f(\theta) = 1 - \exp \left(\frac{-0.5LAI}{\cos\theta} \right) \tag{16}$$

$$T_{rad} = \left[f(\theta)T_c^4 + [1 - f(\theta)] T_s^4 \right]^{\frac{1}{4}}, \tag{17}$$

where θ is the view zenith angle, r_{ah} is the aerodynamic resistance to heat transfer between the canopy and the reference height (see Appendix A of Morillas *et al.* [13]), and r_s is the aerodynamic resistance to heat flow in the boundary layer immediately above the soil surface (see Appendix C of Norman *et al.* [5]).

T_c and T_s are critical for solving the TSEB model and can be measured directly from appropriate measurements. However, ground-based observations are difficult over a large region. Norman *et al.* [5] proposed a method that uses the Priestley-Taylor approach to provide an initial estimate of LE_c as follows:

$$LE_c = \alpha_{pt} f_g \frac{\Delta}{\Delta + \gamma} R_{nc} \tag{18}$$

$$R_{nc} = R_n [1 - \exp(-kLAI / \sqrt{2\cos(\theta_z)})]. \tag{19}$$

Equation (19) is a modification from the original formulation proposed by Norman *et al.* [5] based on simulations with a detailed soil–plant–atmosphere model, Cupid [26]. θ_z is the solar zenith angle and the value of $k = 0.45$ is used for dense vegetated cover (*i.e.*, $LAI \geq 2$), while for partial canopy cover where $LAI < 2$, $k = 0.8$ is used [26]. The green canopy fraction f_g was computed according to Equation (20) [27,28]. f_{IPAR} is estimated as a linear function of NDVI according to Fisher *et al.* [27].

$$f_g = \frac{f_{APAR}}{f_{IPAR}} \tag{20}$$

The parameter α_{pt} is always set as 1.3. By combining Equations (9), (10), (14) and (18), the initial T_c can be obtained. T_s is estimated from this initial T_c by Equation (17), and H_s is estimated by Equation (15). Finally, the initial LE_s can be obtained by Equation (8). This equation system is the basis of the iterative procedure. When the LE_s is greater than zero, iteration stops because a reliable solution has been reached. In contrast, when the LE_s is less than zero, an unrealistic situation under daytime conditions is assumed because condensation in the soil is very unlikely [13]. This is considered in the case of vegetative stress (water or temperature), which forces an iterative reduction of the parameter α_{pt} until a positive LE_s is attained. The Priestley-Taylor approach is relatively simple and has been proven to be theoretically robust for estimates of potential evapotranspiration.

In this study, two more plant physiological constraints, the plant moisture constraint f_m and the plant temperature constraint f_T , were used to reduce the LE_c from its potential level [27,28].

$$LE_c = \alpha_{PT} f_g f_M f_T \frac{\Delta}{\Delta + \gamma} R_{nc} \tag{21}$$

The plant moisture constraint, f_m , was estimated from the relative change in light absorptance according Equation (22), assuming that light absorptance varies primarily in response to moisture stress [29]. f_{ARAR} is the fraction of absorbed photosynthetically active radiation and can be acquired from MODIS standard products or calculated as a function of vegetation indexes [28].

$$f_M = \frac{f_{APAR}}{f_{APARmax}} \tag{22}$$

The plant temperature constraint (f_T) accounts for reductions in the photosynthetic efficiency when plants are growing at temperatures departing from their optimum temperature range [30]. f_T depends on the optimum air temperature for plant growth T_{opt} (°C) and air temperature (T_a). In our research, we fixed T_{opt} as 25 °C, as this value has been applied in global modeling studies across different types of biomes [28]. f_T is given by:

$$f_T = 1.184 \cdot \left[1 + e^{0.2 \cdot (T_{opt} - 10 - T_a)} \right]^{-1} \left[1 + e^{0.3 \cdot (-T_{opt} - 10 - T_a)} \right]^{-1} . \tag{23}$$

The daily ET (ET_{24} , mm) was computed using a method of extrapolation by combining the instantaneous evaporative fraction (EF) derived from ASTER images and the daily radiation ($R_{n,24}$) measured by the micrometeorological flux tower. L is the latent heat of vaporization.

$$ET_{24} = EF \frac{R_{n,24}}{L} = \frac{LE}{R_n - G} \frac{R_{n,24}}{L} \tag{24}$$

3. Results and Discussion

3.1. Surface Radiometric Temperature

Figure 3 depicts a comparison of the ground-based surface radiometric temperatures (T_{rad}) with the ASTER-derived surface temperatures. Although the ASTER images have a spatial resolution of 90 m for the thermal infrared bands and the scale of the thermal ground-based measurements is approximately 10 m [16], the comparison shows reasonable variation, with a determination coefficient of $R^2 = 0.91$, yielding a bias of 0.18 K, an RMSD of 1.10 K, and an MAPD of 0.33%.

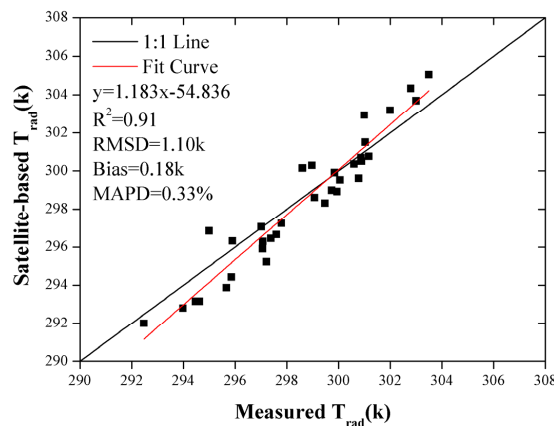


Figure 3. Scatterplot of the ASTER-derived surface radiometric temperatures *versus* surface temperatures measured by infrared thermometers at the study field.

3.2. Instantaneous Surface Energy Fluxes

The estimates of the energy balance components (R_n , G , H , and LE) obtained by combining the modified TSEB model with the ASTER images were compared with the tower-based flux measurements that were adjusted for energy balance closure using the Bowen ratio method. For each flux tower, the simulated fluxes were averaged over the estimated upwind footprint or source area [31]. The following three statistical parameters were chosen to measure the strength of the relationship between the simulated results and measurements: the root mean squared difference (RMSD), bias, and mean absolute percentage difference (MAPD). Maps of the different energy balance terms obtained on 18 August from the application of the improved TSEB models are shown in Figure 4, with the scatterplot shown in Figure 5 and the statistics listed in Table 1. The results indicate that, in general, all four components of the energy balance equation agree reasonably well with the tower-based measurements.

To estimate the net radiation, Equation (10) was applied using values $\epsilon_c = 0.985$ and $\epsilon_s = 0.960$, yielding a bias of $2.4 \text{ W} \cdot \text{m}^{-2}$, $\text{RMSD} = 19.0 \text{ W} \cdot \text{m}^{-2}$ and $\text{MAPD} = 2.2\%$. In some studies, C_g is set as a constant to estimate the soil heat flux; however, C_g can vary within the range 0.2–0.5 depending on the soil type and moisture content. The simulated G from the phase difference equation compares well with the ground measurement, with an RMSD of $17.3 \text{ W} \cdot \text{m}^{-2}$, a bias of $-0.1 \text{ W} \cdot \text{m}^{-2}$, and a MAPD of 18.1%.

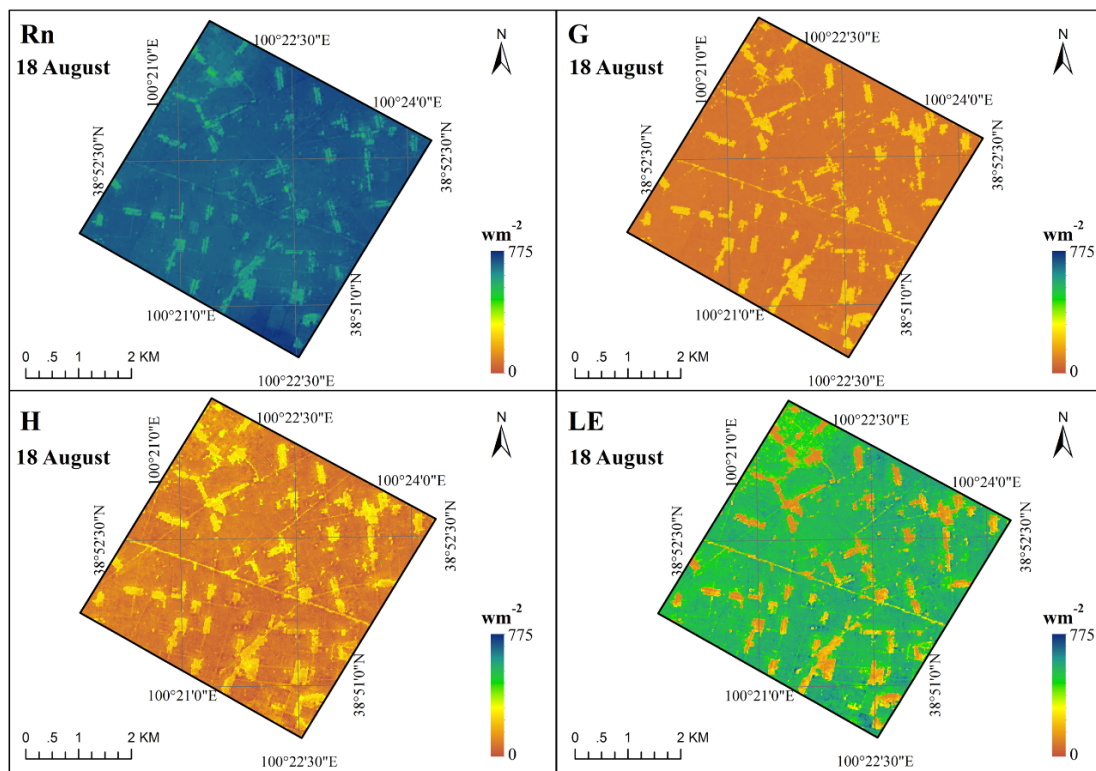


Figure 4. Maps of the improved TSEB-derived surface energy fluxes on 18 August 2012.

Table 1. Statistics of the improved TSEB model-derived surface energy fluxes.

Flux	Day	Observation Number	Observed Averaged ($W \cdot m^{-2}$)	Simulated Averaged ($W \cdot m^{-2}$)	Bias ($W \cdot m^{-2}$)	RMSD ($W \cdot m^{-2}$)	MAPD (%)
Rn	11 August	8	653.4	661.0	7.6	22.1	2.8
	18 August	9	671.3	675.7	4.4	15.1	1.9
	3 September	9	666.4	662.2	−4.2	26.3	3.3
	12 September	9	659.1	660.8	1.7	6.9	0.9
	Overall	35	662.5	664.9	2.4	19.0	2.2
G	11 August	8	80.0	77.7	−2.3	17.8	17.1
	18 August	9	75.2	75.1	−0.1	16.7	20.7
	3 September	9	80.2	77.3	−2.9	23.5	25.9
	12 September	9	74.6	79.5	4.9	7.1	8.6
	Overall	35	77.5	77.4	−0.1	17.3	18.1
H	11 August	8	111.5	116.6	5.1	27.0	25.8
	18 August	9	100.7	104.1	3.4	22.8	18.7
	3 September	9	200.1	189.1	−11.0	24.3	10.2
	12 September	9	282.3	278.5	−3.8	46.8	13.2
	Overall	35	173.7	172.1	−1.6	31.9	16.7
LE	11 August	8	461.9	466.7	4.8	38.2	6.4
	18 August	9	495.3	496.4	1.1	25.0	3.9
	3 September	9	386.1	395.9	9.8	22.2	4.7
	12 September	9	302.2	302.8	0.6	48.6	13.5
	Overall	35	411.4	415.5	4.1	35.1	7.1

Figure 5 shows high values of the determination coefficient R^2 for both the simulated H and LE compared to the tower-based flux measurements. H had an RMSD of $31.9 W \cdot m^{-2}$, a bias of $-1.6 W \cdot m^{-2}$, and a MAPD of 16.7%. LE was also well reproduced by the improved TSEB model, demonstrating an overall RMSD of $35.1 W \cdot m^{-2}$, a bias of $4.1 W \cdot m^{-2}$ and a MAPD of 7.1%. An obvious seasonal change is evident from the mean values of H and LE from Table 1. For 11 August and 18 August, both the simulated and measured sensible heat flux showed a mean value over all stations of approximately $100 W \cdot m^{-2}$, with relatively high latent heat flux mean values. However, in September, the corn began to transition into its senescence stage, and the vegetative stress condition decreases the latent heat to less than $400 W \cdot m^{-2}$ and increases the sensible heat flux to over $200 W \cdot m^{-2}$ for both days.

Figure 6 presents comparisons of the H and LE from the original and improved TSEB models. The original TSEB model without the constraints f_i and f_m tended to overestimate the latent heat flux and underestimate the sensible heat flux. Figure 7 shows the mean values of H and LE for the four days, obtained using the two approaches. On 18 August, the sensible heat flux from the original TSEB was slightly less than the EC measurements. However, on 11 August, 3 September, and 12 September, H was underestimated by the original approach, leading to overestimation of LE .

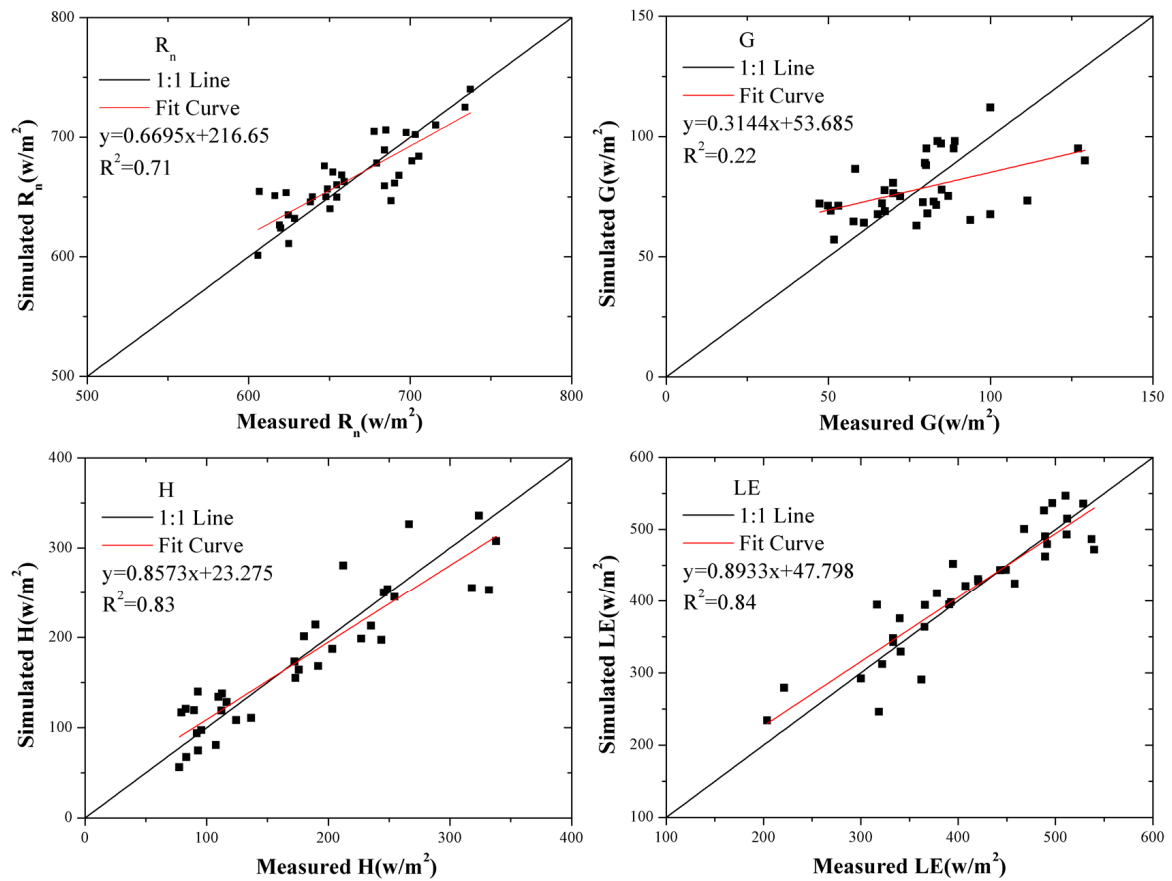


Figure 5. Scatterplots of the improved TSEB-derived energy fluxes *versus* EC tower-based measurements.

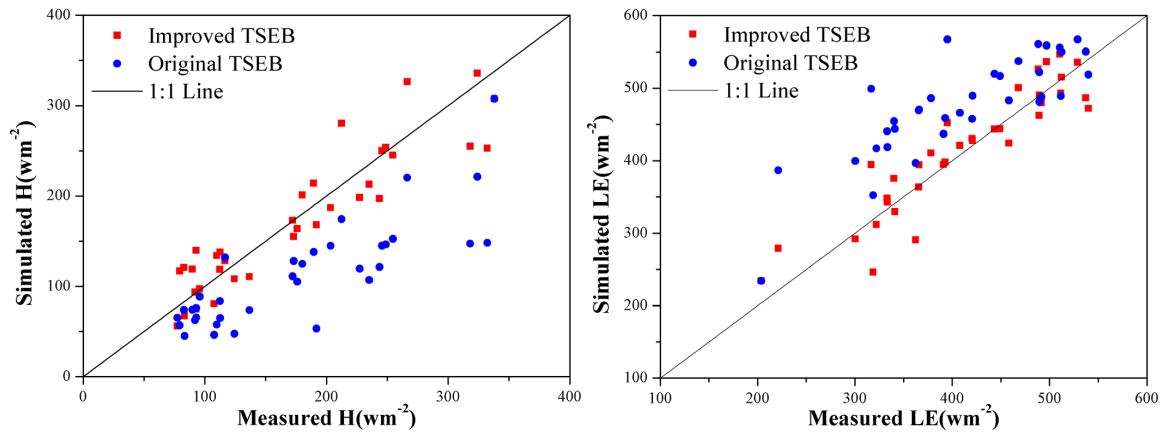


Figure 6. Comparisons of the sensible and latent heat fluxes obtained from the improved and original TSEB models with tower-based measurements.

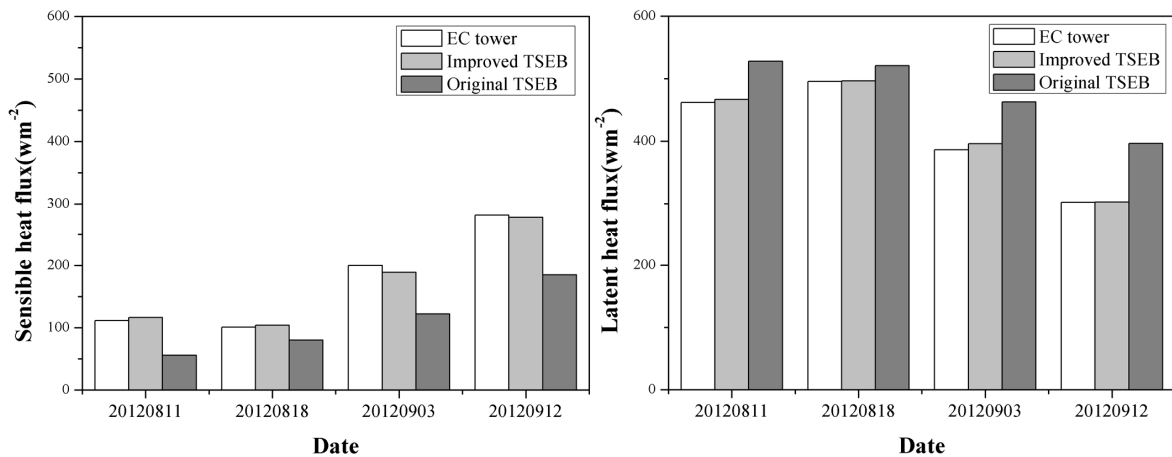


Figure 7. Mean sensible and latent heat fluxes for the tower locations derived from the improved TSEB, original TSEB, and EC tower measurements.

3.3. Daily ET

Figure 8 presents comparisons of the model-derived and tower-based measurements, and Figure 9 shows maps of the daily ET for the four days. The ET maps for the four days indicate both temporal and spatial variations. The corn field showed higher ET values than the other land use types. A seasonal variation in ET was also found; an obvious decline in ET occurred in September because the vegetation transitioned into the senescent stage, with more severe vegetative stress. The results from the improved TSEB model showed good overall agreement with the ET measured by eddy covariance. Although some adjacent values were found for both the improved and original TSEB models, the latter generally overestimated ET, especially on 11 August, 3 September, and 12 September (Figure 10). From the statistics in Table 2, larger RMSD, bias, and MAPD values were obtained using the original TSEB. The improved TSEB model, including consideration of the physiological constraints, provided a more reasonable estimation of the daily ET, decreasing the overall RMSD by approximately 0.44 mm, the bias by 0.59 mm, and the MAPD by 11.53%.

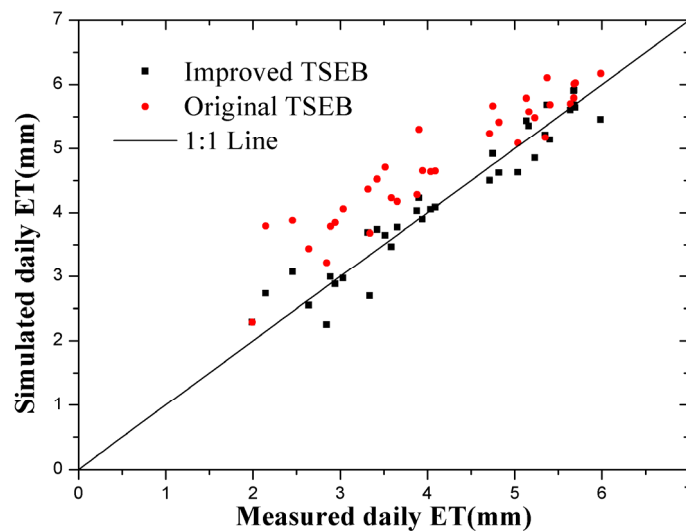


Figure 8. Comparison of the daily ET derived from the improved and original TSEB with EC tower-based measurements.

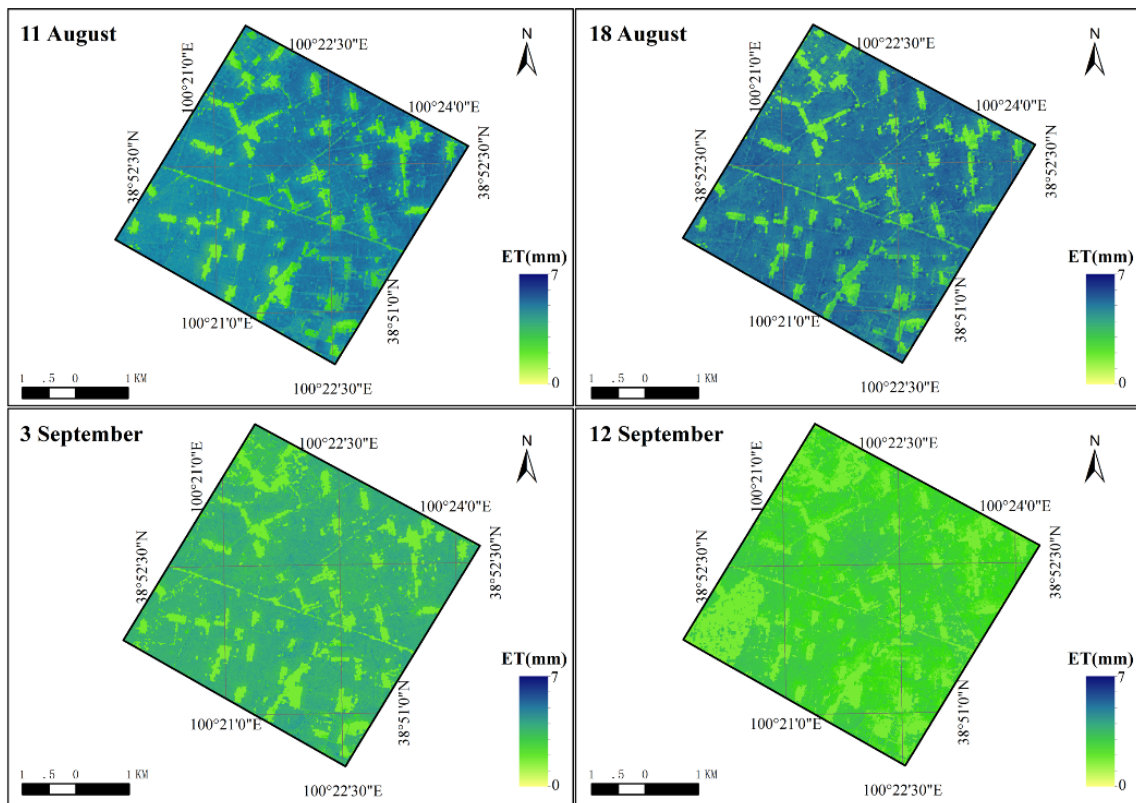


Figure 9. Maps of the daily ET from ASTER images for four days: 11 August, 18 August, 3 September, and 12 September.

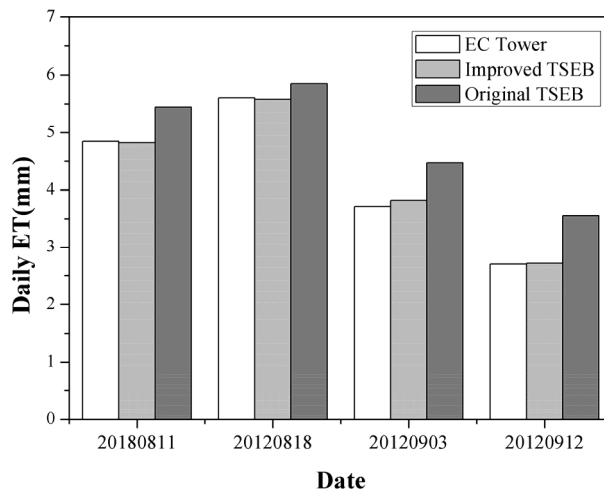


Figure 10. Mean daily ET for the tower locations derived from the improved TSEB, original TSEB, and EC tower.

Table 2. Statistics of improved and original TSEB model-derived daily ET.

Model	RMSD (mm)	BIAS (mm)	MAPD (%)
Improved TSEB	0.30	0.02	6.63
Original TSEB	0.74	0.61	18.16

3.4. Determination of the Effects of Plant Constraints

Reliable ET estimates are essential for improving spatial crop water management. Land surface energy balance models, using remote sensing data from ground to airborne and satellite platforms at different spatial resolutions, have been found to be promising for mapping daily ET at the farm level and on the regional scale [16]. Recent research has shown that the TSEB model solved using the original Priestley-Taylor approach may overestimate LE , especially under low soil wetness, high air drying power, and sparse vegetation cover [11,13–15]. The parameter α_{pt} of 1.3 is suitable for unstressed canopy [31], however, there is a critical assumption involved in TSEB that the Priestley-Taylor formula with only f_g and a parameter α_{pt} of 1.3 applies for both stressed and unstressed vegetation and agricultural crops, and there is no mechanism in the model to capture the condition of $\alpha_{pt} < 1.3$ and $LE_s > 0$. Examining the Priestley-Taylor iteration approach in TSEB, the parameter α_{pt} is only manually reduced to account for vegetative stress when a nonphysical solution of LE_s , i.e., $LE_s < 0$ during the daytime, is attained. Therefore, if a solution, i.e., $LE_s > 0$, is obtained under vegetative stress, the parameter α_{pt} does not change, and overestimation of LE occurs. Furthermore, when reducing α_{pt} , the iteration immediately stops when LE_s is above zero; however, it is unreasonable sometimes because α_{pt} may still be too large.

f_g accounts for the fraction of the LAI that is green and is assumed to be unified without additional information about phenological condition [5]. The method for f_g in this paper has been widely used in regional estimates of actual evapotranspiration and has also been validated for different ecosystems [13,27,28]. Fisher *et al.* [27] proposed that no moisture stress occurs before peak light absorbance, when the canopy is actively growing and water stress should be minimal. At moist sites, f_m plays only a minor role; its contribution is primarily limited to sites that experience drought. The method for f_t is from the Carnegie–Ames–Stanford Approach (CASA) model [28]. f_t decreases when the air temperature departs from the optimum range for plants growth. To avoid calibrations of T_{opt} depending on the site, Garcia *et al.* [28] fixed T_{opt} at 25 °C, a value that has been widely applied.

To determine the relationships between plant constraints and derived energy fluxes, we determined the mean values for the three plant constraints (Table 3). f_g changed slightly for the four days, and f_m and f_t varied daily. On 18 August, f_m is the largest of the four days and f_t values were close to 1; thus, the performance of the two approaches was more similar. For 11 August, TSEB without an f_t close to 1 and a decreasing f_m (0.72) underestimated H (Figure 7). On 3 September and 12 September, both f_m and f_t declined because of increasing plant moisture and temperature stress. In this situation, the canopy is less vigorous, with a higher canopy resistance; the stomata of leaves near the top of the canopy close progressively, and plants start to reduce their transpiration. More energy is transformed into sensible heat flux. If the vegetative stress becomes more severe, sensible heat flux can become the dominant turbulent heat flux; this phenomenon is found in the drylands in the arid region.

Ignoring f_m and f_t , the simulated H of the two days in September was lower than the EC measurements, causing an overestimation of the latent heat flux, especially on 12 September (Figure 7). This overestimation was a result of the more severe vegetative stress that occurs, with lower f_m and f_t .

Table 3. Mean values of f_g , f_m and f_t .

Date	f_g	f_m	f_t
11 August	0.96	0.72	1.00
18 August	0.98	0.82	0.99
3 September	0.95	0.70	0.81
12 September	0.88	0.51	0.52

Guzinski *et al.* [32] found that the TSEB model is sensitive to α_{pt} and that using only the remote sensing vegetation-index-based f_g to scale α_{pt} may lead to an underestimation of the sensible heat flux. As Consoli and Vanella [16] proposed that the α_{pt} variation should be set within the range of 1.1 to 1.3, a lower value $\alpha_{pt} = 1.1$ was also tested for the original TSEB model. Although better results were found from the comparison of averaged heat fluxes, the phenomenon of the original TSEB with $\alpha_{pt} = 1.1$ underestimating H and overestimating LE still existed, especially in September (Table 4). Manually adjusting the value of α_{pt} downwards may play a role under multiple vegetative stress conditions; however, this seems subjective because the severity of vegetative stress is always not clear. Using plant physiological-based different constraints may be more reasonable.

The described satellite-based energy balance models provide instantaneous values for the heat flux corresponding to the time of satellite overpass. An important step in the application of the improved two-source energy balance model is extrapolation from instantaneous to daily data, which are more valuable for agricultural purposes. The extrapolation method used in this paper assumes self-preservation in the diurnal cycle of the energy budget, such that the relative partitioning among the components of the energy balance, expressed by EF, remains constant throughout the day. In this method, the accuracy of the instantaneous EF directly determines the precision of the daily ET. Overestimation of the instantaneous latent heat flux in the original TSEB model also results in overestimation of the EF, leading to obviously higher daily ET measurements than EC measurements, especially under severe vegetative stress, as shown by the reduced f_m and f_t values in September. The comparison indicated that the improved TSEB model provided a more accurate estimation of the daily ET than the original TSEB.

Table 4. Statistics of energy fluxes from improved TSEB and original TSEB ($\alpha_{pt} = 1.3$ and 1.1).

Flux	Day	Observed Averaged ($W \cdot m^{-2}$)	Improved TSEB Averaged ($W \cdot m^{-2}$)	Original TSEB Averaged ($W \cdot m^{-2}$)	TSEB ($\alpha_{pt} = 1.1$) Averaged ($W \cdot m^{-2}$)
H	11 August	111.5	116.6	55.6	78.1
	18 August	100.7	104.1	80.1	94.9
	3 September	200.1	189.1	122.2	141.9
	12 September	282.3	278.5	184.8	199.4
LE	11 August	461.9	466.7	527.7	505.2
	18 August	495.3	496.4	520.5	505.7
	3 September	386.1	395.9	462.8	443.0
	12 September	302.2	302.8	396.6	381.9

Many single-source models, such as SEBS and SEBAL, also underestimate the sensible heat flux, especially over a partial canopy. Gokmen *et al.* [6] were the first to propose considering the water stress and integrating the soil moisture factor derived from remote sensing data into SEBS; however, the fitting method is complex, limited, and difficult to extend over a large area. On the other hand, the improved approach in this study requires no calibration and can be easily applied with imagery from many other satellites with thermal infrared bands, such as MODIS, FY3, and Landsat, for regional, continental, or global mapping of ET . A comparison of a single-source model and improved TSEB may be conducted in a future study. The TSEB-based dual temperature difference (DTD) model, introduced by Norman *et al.* [26], will also be tested with the improved TSEB in future work.

4. Conclusions

The main aim of this study was to test an improved TSEB model that takes into account plant physiological, moisture, and temperature constraints. We have found that the original TSEB model overestimates the latent heat flux under multiple vegetative stresses (moisture and air temperature), as previously reported. The estimates of the surface energy fluxes obtained by combining the

improved TSEB with ASTER images and meteorological data were compared with measurements obtained from nine eddy covariance towers. More accurate sensible and latent heat estimates were found, even under severe vegetative stress conditions. The proposed approach can easily be used with other satellite images for a larger area of application.

Acknowledgments: This research was supported by the National Natural Sciences Foundation of China (41271424). The meteorological and remote sensing data were provided by the HiWATER project and the Cold and Arid Regions Science Data Center at Lanzhou (<http://westdc.westgis.ac.cn>).

Author Contributions: Qifeng Zhuang contributed to designing the experiment, putting it into context, analyzing the results, preparing the figures and maps, and writing the final manuscript. Bingfang Wu contributed to describing the TSEB model, data collection, and data processing.

Conflicts of Interest: The authors declare that no conflicts of interest exist.

References

1. Merlin, O.; Chirouze, J.; Olioso, A.; Jarlan, L.; Chehbouni, G.; Boulet, G. An image-based four-source surface energy balance model to estimate crop evapotranspiration from solar reflectance/thermal emission data (SEB-4S). *Agric. For. Meteorol.* **2014**, *184*, 188–203. [[CrossRef](#)]
2. Bastiaanssen, W.G.M.; Menenti, M.; Feddes, R.A.; Holtslag, A.A.M. A remote sensing surface energy balance algorithm for land (SEBAL): 1. Formulation. *J. Hydrol.* **1998**, *212–213*, 198–212. [[CrossRef](#)]
3. Allen, R.G.; Tasumi, M.; Trezza, R. Satellite-based energy balance for mapping evapotranspiration with internalized calibration (METRIC)-model. *J. Irrig. Drain. Eng.* **2007**, *133*, 380–394. [[CrossRef](#)]
4. Su, Z. The surface energy balance system (SEBS) for estimation of turbulent heat fluxes. *Hydrol. Earth Syst. Sci.* **2002**, *6*, 85–99. [[CrossRef](#)]
5. Norman, J.M.; Kustas, W.P.; Humes, K.S. Source approach for estimating soil and vegetation energy fluxes in observations of directional radiometric surface temperature. *Agric. For. Meteorol.* **1995**, *77*, 263–293. [[CrossRef](#)]
6. Gokmen, M.; Vekerdy, Z.; Verhoef, A.; Verhoef, W.; Batelaan, O.; van der Tol, C. Integration of soil moisture in SEBS for improving evapotranspiration estimation under water stress conditions. *Remote Sens. Environ.* **2012**, *121*, 261–274. [[CrossRef](#)]
7. Paul, G.; Gowda, P.H.; Prasad, P.V.V.; Howell, T.A.; Aiken, R.M.; Neale, C.M.U. Investigating the influence of roughness length for heat transport (z_{oh}) on the performance of SEBAL in semi-arid irrigated and dryland agricultural systems. *J. Hydrol.* **2014**, *509*, 231–244. [[CrossRef](#)]
8. Lhomme, J.P.; Chehbouni, A. Comments on dual-source vegetation-atmosphere transfer models. *Agric. For. Meteorol.* **1999**, *94*, 269–273. [[CrossRef](#)]
9. Sanchez, J.M.; Kustas, W.P.; Caselles, V.; Anderson, M. Modelling surface energy fluxes over maize using a two-source patch model and radiometric soil and canopy temperature observations. *Remote Sens. Environ.* **2008**, *112*, 1130–1143. [[CrossRef](#)]
10. Anderson, M.C.; Norman, J.M.; Kustas, W.P.; Houborg, R.; Starks, P.J.; Agam, N. A thermal-based remote sensing technique for routine mapping of land-surface carbon, water and energy fluxes from field to regional scales. *Remote Sens. Environ.* **2008**, *112*, 4227–4241. [[CrossRef](#)]
11. Long, D.; Singh, V.P. A Two-source Trapezoid Model for Evapotranspiration (TTME) from satellite imagery. *Remote Sens. Environ.* **2012**, *121*, 370–388. [[CrossRef](#)]
12. Kustas, W.P.; Norman, J.M. A two-source approach for estimating turbulent fluxes using multiple angle thermal infrared observations. *Water Resour. Res.* **1997**, *33*, 1495–1508. [[CrossRef](#)]
13. Morillas, L.M.; Villagarcia, L.; Domingo, F.; Nieto, H.; Ucles, O.; Garcia, M. Environmental factors affecting the accuracy of surface fluxes from a two-source model in Mediterranean drylands: Upscaling instantaneous to daytime estimates. *Agric. For. Meteorol.* **2014**, *189–190*, 140–158. [[CrossRef](#)]
14. Li, F.Q.; Kustas, W.P.; Prueger, J.H.; Neale, C.M.U.; Jackson, T.J. Utility of remote sensing-based two-source energy balance model under low- and high-vegetation cover conditions. *J. Hydrometeorol.* **2005**, *6*, 878–891. [[CrossRef](#)]
15. Gonzalez-Dugo, M.P.; Neale, C.M.U.; Mateos, L.; Kustas, W.P.; Prueger, J.H.; Anderson, M.C.; Li, F. A comparison of operational remote sensing-based models for estimating crop evapotranspiration. *Agric. For. Meteorol.* **2009**, *149*, 1843–1853. [[CrossRef](#)]

16. Consoli, S.; Vanella, D. Comparisons of satellite-based models for estimating evapotranspiration fluxes. *J. Hydrol.* **2014**, *513*, 475–489. [[CrossRef](#)]
17. Liu, S.M.; Xu, Z.W.; Zhu, Z.L.; Jia, Z.Z.; Zhu, M.J. Measurements of evapotranspiration from eddy-covariance systems and large aperture scintillometers in the Hai River Basin, China. *J. Hydrol.* **2013**, *487*, 24–38. [[CrossRef](#)]
18. Twine, T.E.; Kustas, W.P.; Norman, J.M.; Cook, D.R.; Houser, P.R.; Meyers, T.P.; Prueger, J.H.; Starks, P.J.; Wesely, M.L. Correcting eddy-covariance flux underestimates over a grassland. *Agric. For. Meteorol.* **2000**, *103*, 279–300. [[CrossRef](#)]
19. Wang, Y.Y.; Li, X.X.; Tang, S.H. Validation of the SEBS-derived sensible heat for FY3A/VIRR and TERRA/MODIS over an alpine grass region using LAS measurements. *Int. J. Appl. Earth Obs.* **2013**, *23*, 226–233. [[CrossRef](#)]
20. Jimenez-Munoz, J.C.; Sobrino, J.A. Feasibility of retrieving land-surface temperature from ASTER TIR bands using two-channel algorithms: A case study of agricultural areas. *IEEE Geosci. Remote Sens. Lett.* **2007**, *4*, 60–64. [[CrossRef](#)]
21. Kustas, W.; Norman, J.; Anderson, M.; French, A. Estimating subpixel surface temperatures and energy fluxes from the vegetation index-radiometric temperature relationship. *Remote Sens. Environ.* **2003**, *85*, 429–440. [[CrossRef](#)]
22. Mira, M.; Valor, E.; Boluda, R.; Caselles, V.; Coll, C. Influence of soil water content on the thermal infrared emissivity of bare soils: Implication for land surface temperature determination. *J. Geophys. Res.* **2007**, *112*. [[CrossRef](#)]
23. Rubio, E.; Caselles, V.; Coll, C.; Valour, E.; Sospedra, F. Thermal-infrared emissivities of natural surfaces: Improvements on the experimental set-up and new measurements. *Int. J. Remote Sens.* **2003**, *24*, 5379–5390. [[CrossRef](#)]
24. Consoli, S.; D’Urso, G.; Toscano, A. Remote sensing to estimate ET-fluxes and the performance of an irrigation district in southern Italy. *Agric. Water Manag.* **2006**, *81*, 295–314. [[CrossRef](#)]
25. Colaizzi, P.D.; Kustas, W.P.; Anderson, M.C.; Agam, N.; Tolch, J.A.; Evett, S.R.; Howell, T.A.; Gowda, P.H.; O’Shaughnessy, S.A. Two-source energy balance model estimates of evapotranspiration using component and composite surface temperatures. *Adv. Water Resour.* **2012**, *50*, 134–151. [[CrossRef](#)]
26. Norman, J.M.; Kustas, W.P.; Prueger, J.H.; Diak, G.R. Surface flux estimation using radiometric temperature: A dual-temperature-difference method to minimize measurement errors. *Water Resour. Res.* **2000**, *36*, 2263–2274. [[CrossRef](#)]
27. Fisher, J.B.; Tu, K.P.; Baldocchi, D.D. Global estimates of the land–atmosphere water flux based on monthly AVHRR and ISLSCP-II data, validated at 16 FLUXNET sites. *Remote Sens. Environ.* **2013**, *112*, 901–919. [[CrossRef](#)]
28. Garcia, M.; Sandholt, I.; Ceccato, P.; Ridler, M.; Mougou, E.; Kergoat, L.; Morillas, L.; Timouk, F.; Fensholt, R.; Domingo, F. Actual evapotranspiration in drylands derived from *in situ* and satellite data: Assessing biophysical constraints. *Remote Sens. Environ.* **2013**, *131*, 103–118. [[CrossRef](#)]
29. Myneni, R.B.; Williams, D.L. On the relationship between FAPAR and NDVI. *Remote Sens. Environ.* **1994**, *49*, 200–211. [[CrossRef](#)]
30. Yuan, W.P.; Liu, S.G.; Yu, G.R.; Bonnefond, J.M.; Chen, J.Q.; Davis, K.; Desai, A.R.; Goldstein, A.H.; Gianelle, D.; Rossi, F.; *et al.* Global estimates of evapotranspiration and gross primary production based on MODIS and global meteorology data. *Remote Sens. Environ.* **2010**, *114*, 1416–1431. [[CrossRef](#)]
31. Choi, M.; Kustas, W.P.; Anderson, M.C.; Allen, R.G.; Li, F.Q.; Kjaersgaard, J.H. An intercomparison of three remote sensing-based surface energy balance algorithms over a corn and soybean production region (Iowa, US) during SMACEX. *Agric. For. Meteorol.* **2009**, *149*, 2082–2097. [[CrossRef](#)]
32. Guzinski, R.; Anderson, M.C.; Kustas, W.P.; Nieto, H.; Sandholt, I. Using a thermal-based two source energy balance model with time-differencing to estimate surface energy fluxes with day-night MODIS observations. *Hydrol. Earth Syst. Sci.* **2013**, *17*, 2809–2825. [[CrossRef](#)]

